PHYSICAL REVIEW B **103**, 214107 (2021)

Role of V-V dimers on structural, electronic, magnetic, and vibrational properties of VO_2 by first-principles simulations and Raman spectroscopic analysis

Wasim Raja Mondal,[1,*] Egor Evlyukhin,[1] Sebastian A. Howard,[1] Galo J. Paez,[1] Hanjong Paik,[2,3] Darrell G. Schlom,[2,4]
Louis F. J. Piper,[1] and Wei-Cheng Lee[1,†]
[1]*Department of Physics, Applied Physics, and Astronomy, Binghamton University, State University of New York, Binghamton, New York 13850, USA*
[2]*Departments of Materials Science and Engineering, Cornell University, Ithaca, New York 14853-1501, USA*
[3]*Platform for the Accelerated Realization, Analysis and Discovery of Interface Materials (PARADIM), Cornell University, Ithaca, New York 14853, USA*
[4]*Kavli Institute at Cornell for Nanoscale Science, Ithaca, New York 14853, USA*

(Received 19 August 2020; revised 13 May 2021; accepted 14 May 2021; published 9 June 2021)

We investigate the vibrational properties of VO_2, particularly the low-temperature M1 phase by first-principles calculations using the density functional theory as well as Raman spectroscopy. In the theoretical aspect, the phonon calculation requires structure optimization and force calculations on a large supercell to obtain an accurate result, and strong correlation effects in VO_2 make this task very challenging. We perform the structural optimization using SCAN meta-GGA functional and obtain the optimized crystal structures with the correct energy hierarchy as well as correct electronic properties for the rutile and M_1 phases of VO_2 including both the nonmagnetic (NM) and antiferromagnetic (AFM) spin ordering. We show both the NM-M_1 and AFM-M_1 are insulators, whereas NM-R and AFM-R are metals. However, FM-R and FM-M_1 are found be same as energetically favorable and becomes half-metal. Based on the harmonic approximation around the optimized structures obtained from the NM calculations at zero temperature, we reproduce the phonon softening in the rutile phase as well as the phonon stiffening in the M_1 phase. Our phonon calculations reveal that both the NM-M_1 phase and AFM-M_1 are dynamically stable, whereas FM-M_1 is found to be dynamically unstable. In addition, we perform Raman experiment on VO_2 thin films which stimulate enormous interests in the field of thin-film engineering for transition metal oxides. We demonstrate from the comparison between theoretical calculations and Raman measurements that the subtle change of the V-V dimer due to the strain effect can be reliably detected by the Raman spectroscopy, which could be a new framework to determine the subtle change of crystal structure for transition metal oxide thin films.

DOI: 10.1103/PhysRevB.103.214107

I. INTRODUCTION

Vanadium oxide (VO_2) has been a focus of intense research since its discovery in 1959 [1]. Besides academic interest, it underpins a plethora of applications including gas sensors [2], window coatings [3], resistive random access memory (RRAM) devices [4], electronic switches [5–7], and so on. The versatile phase diagram of VO_2 showcase well known first order metal-insulator transition (MIT) at almost room temperature (340 K) and ambient pressure accompanied by a structural transition from a high-temperature and high-symmetry rutile (R phase) to a low-temperature and low-symmetry monoclinic (M_1 phase). Due to this intricate concomitant nature of these two transitions, the controversy between predicting the accurate structural properties and accurate electronic properties has not been still completely resolved. Strong electron correlations has been believed to be a key mechanism for explaining large energy gap of 0.7 eV in the insulating M_1 phase of VO_2 [8–10]. Several other proposals suggest that the electron correlations may not be good enough and the structural properties should be also taken into account in combination with the strong electron correlations effects for more complete description of the VO_2[11–13]. Though extensively studied, a consensus for a exact mechanism of MIT in VO_2 is still elusive. Overall, extensive research indicate that the role of structural properties can not be underestimated in explaining the rich phase diagram of VO_2 [14–16].

The role of defects, vacancies, doping and, strain in this phase diagram has been an ongoing topic of research in recent time [17]. For example, Wickramaratne *et al.* [18] find that the V Frenkel defects in the insulating phase of VO_2 can reduce resistivity compared to pristine VO_2. Using diffusion Monte Carlo, Ganesh *et al.* [19] show that the gap in the M_1 phase can be suppressed by doping with the oxygen vacancies. Several investigations suggest that strain can greatly influence the MIT mechanism [20–23]. Therefore, the structural properties should be investigated more carefully and lattice vibrational properties of VO_2 can give us a new insight of its structure.

---

[*] wmondal@binghamton.edu
[†] wlee@binghamton.edu

However, achieving an accurate description of the lattice vibrational properties of the VO_2 turns out to be a nontrivial task from both the experimental and theoretical point of view. For example, the bottleneck of single-crystal inelastic neutron scattering (INS) is the incoherent vanadium neutron scattering cross-section. Even, some of the existing Raman spectroscopic studies of the structural phase transition (SPT) in epitaxial VO_2 films have been found to be inconsistent due to the large thicknesses of studied films (80–100 nm) or even misinterpreted due to the strong signals from the substrate [24–27].

Besides these experimental challenges, achieving an exact theoretical description of the lattice dynamics of VO_2 has been a tougher nut to crack. Since lattice vibrational properties are strongly related with the structure of the material, first-principles-based methods that take into account the much needed material specific information can be an ideal tool for this task. However, a reliable exchange functional which can correctly describe the vibrational properties of all the phases of VO_2 is not readily available and still an going topic of research. It has been found that the standard functional such as local density approximation (LDA) and generalized gradient approximations (GGA) can not describe the structural, electronic and magnetic features of the R and M_1 phases simultaneously [15,28]. Thus, the LDA and GGA-based calculations clearly manifest the well known "band gap" problem in DFT.

To ameliorate this "band gap" issue, several attempts have been already made to go beyond the LDA or GGA functional. For example, the modified Becke-Johnson (mBJ) exchange potential has been demonstrated to be very efficient for describing the MIT in VO_2 [28]. The GW method and its variants successfully predict the electronic feature of the MIT [29–31]. The dynamical mean-field theory and its cluster extensions correctly describe the electronic properties of both the R and M_1 phases of VO_2 [11,32]. Moreover, hybrid functionals efficiently describe the electronic properties of VO_2 [33] and is found to be also successful in describing the structural properties of all the phases of VO_2 [34]. First-principles-based quantum Monte Carlo-based calculations have been also performed for VO_2 [35]. Unfortunately, all these efforts fall short for the phonon calculations of VO_2.

For example, the Hellmann–Feynman force calculations are not possible using the mBJ ruling out the possibility of phonon calculations within this exchange approximation. Phonon calculations using the GW formalism has not been formulated yet. Cluster extension of DMFT such as dynamical cluster approximations (DCA) and its typical medium extension named as typical medium DCA (TMDCA) for disordered phononic systems has been recently developed [36,37]. Unfortunately, such DCA and TMDCA method for phononic systems are currently available for parameter-based model calculations. Phonon calculations using hybrid functionals turn out to be not a practical approach due to computational expenses.

Considering all these limitations, the GGA + U method [38–41] has been extensively used for phonon calculations of VO_2 because it is claimed to resolve the "band gap" problem and at the same time it is computationally less expensive. However, the GGA + U method remains controversial in producing an accurate description of VO_2. Anisimov and coauthors [38] find insulating nature of the R phase which strongly disagree with experimental findings. Mellan *et al.* [40] predict electronic structure of VO_2 that is consistent with experiment using nonspin polarised GGA + U calculations. But, U value within the LDA + U method has been treated so far as a free parameter and the results are also very sensitive with the choice of U value. For example, Budai *et al.* [41] point out that the U value less than 3.4 eV is more appropriate in determining energy difference between the R and M_1 phase that could be more consistent with experiment, but such lower U value can produce more smaller bandgap. Hence, an accurate prediction of the U value rather using it as a free parameter or bare atomic value, may have a paramount importance for reliable estimation of the vibrational properties of VO_2. To best of our knowledge, calculations for determining U value of VO_2 via the constrained random phase approximation (cRPA) or linear response method are still missing. Another important thing is to include temperature effect and anharmonicity in phonon calculations. Such calculations [41] have been already performed and can help to validate further theoretical development.

Besides the "band gap" problem, another challenge is to predict the correct magnetic structure of VO_2. The magnetic ground state of the Mott-Hubbard insulators generally shows antiferromagnetic order. However, VO_2 is a prototypical example of strongly correlated system whose magnetic ground state is a spin singlet (nonmagnetic)[NM]. The R phase is experimentally found to be paramagnetic above the transition temperature of 340 K [42,43]. While the M_1 phase is found to be NM [44], the $S = \frac{1}{2}$-Heisenberg chains are believed to characterizing the M_2 phase [45].

Cluster DMFT approach does not suffer in predicting the true singlet state. However, it is not practical to use cluster DMFT for large supercells due to computational expenses [11,13]. On the other hand, the DFT like mean-field theory fails to predict a true singlet state. It can only determine a single-determinant state. Again, several efforts have been made by applying the improved functional to predict the correct magnetic ground state. Eyert [33] claims that the screened hybrid functional can provide a good description of the electronic and magnetic structures of VO_2 phases. However, Grau-Crespo *et al.* [46] do not agree with Eyert's results [33] and they find a magnetic ground state for the M_1 phase, a nonmetallic ground state for the R phase, and an R-M1 energy difference in significant disagreement with the experimental latent heat using hybrid functional in their calculations. Other approach like the LDA + U method also suffers in predicting correct magnetic structure of all the phases of VO_2. Mellan *et al.* [40] show that LDA + U can predict correct electronic and magnetic ground state of VO_2 using non-spin-polarized calculations. However, such conclusions do not hold true when spin-polarized calculations are considered. Anisimov *et al.* [38] predict an antiferromagnetic ground state of the M_1 phase using the LDA + U method which is not correct. However, the issue of the hybrid functional considering spins are reexamined by Xu *et al.* [34] and they point out that the results are sensitive to the nature of the pseudopotentials used in the calculations. For example, they show in Ref. [34] that the AFM-M_1 state is metastable if typical oxygen pseudopotentials is used but it becomes unstable if hard potential is considered in the calculations. They show that the calculated total energies according to the AFM-R and NM-R phase are higher than FM-R by 125 and 140 meV per formula unit, respectively [34], and thus FM-R is found to be ground state of the R phase which contradicts with experiment. This recent hybrid functional study show the NM-M_1 phase is more stable compared to the AFM-M_1 phase which is consistent with the experiments [42,43]. Three possible spin configurations, termed as A-AFM, C-AFM and G-AFM are considered to predict the correct antiferromagnetic configurations of the M_2 phase using hybrid functional and both A-type and G-type AFM-M_2 is found to agree with the experimentally derived model in which M_2 is AFM and local magnetic moments exist only on the canted zigzag V-V chains. The Quantum Monte Carlo simulations [35] are also applied to resolve the issue related with spin polarization in the DFT description of VO_2. The accuracy of ab initio electron correlation and electron densities in correctly describing the physics of VO_2 have been investigated in detail in Ref. [47]. In this study, among all the nonhybrids, the SCAN functional turns out to be as nearly balanced in terms of magnetization across the M1-R transition. In addition, it also accurately determine the ground state crystal structure of VO_2. Indeed, predicting accurate magnetic structure of VO_2 including all the phases from band theory is still an open question.

In this paper, we present a comprehensive study of the lattice dynamics and electronic structures using various DFT functionals and benchmark our calculations with experiments. By comparing with Raman spectroscopy, we investigate the interplay between strain effect and local environment (e.g., spectral shifts of the V-V and V-O phonon modes) in epitaxial VO_2 thin films deposited on MgF_2 (001) and (110) substrates. We show that our calculations are in a good agreement with the observed Raman shifts of the characteristic phonon modes induced by the epitaxial strains imposed on VO_2 thin films. Our work demonstrates that Raman spectroscopy could serve as a reliable way to detect the subtle change of V-V dimer in the strained VO_2.

We have organized this paper as follows: we give details of our first-principles simulations in Sec. II. We provide information of our experimental set up in Sec. III. We present and discuss our results in Sec. IV. Finally, we conclude our discussions in Sec. V.

II. COMPUTATIONAL DETAILS

We consider a plane-wave basis and the projector-augmented-wave (PAW) method as implemented in the Vienna Ab initio Simulation Package (VASP) [49,50]. We have used several different exchange correlation functional including the LDA, the PBE GGA [51], and the SCAN [52]. We note that the SCAN has been implemented for self-consistent calculations in the VASP and such self-consistent implementation is still not available in other first-principles packages like WIEN2K. We choose PBE GGA pseudopotential in our calculations using SCAN. For electronic structure calculations, we use the plane-wave cutoff energy as 500 eV. We also verify that there is no appreciable changes in the results using a cutoff energy of 600 eV. For all Brillouin-zone sampling, Γ-centered k-point grids is considered as $16 \times 16 \times 16$. The self-consistent calculations are considered to be converged by considering 10^{-4} eV between successive iterations, and the convergence of structural relaxation is decided by the total energy difference between two successive ionic steps as 10^{-3} eV. We have also cross-checked our electronic structure calculations by using mBJ calculations as available in WIEN2K. The results obtained from the WIEN2K are not shown here. For the phonon calculations, we have employed the pseudopotential band method and the supercell approach that are implemented in VASP [49,50] and PHONOPY [53]. As a standard supercell-based phonon calculations, force-constants are computed by means of the Hellmann-Feynman theorem [54].

III. EXPERIMENTAL DETAILS

High-quality 10-nm-thick VO_2 films were grown on rutile MgF_2 (001) and (110) single crystal substrates by reactive molecular-beam epitaxy (MBE) via codeposition method under a distilled ozone background pressure at the PARADIM Thin Film Growth Facility at Cornell university [55]. Raman microscopy analysis was conducted at the Center for Nanoscale Materials at the Argonne National Laboratory. The spectra were recorded using a Raman microscope (inVia Reflex, Renishaw, Inc.) with spectral resolution of 0.5 cm^{-1} using 532 nm excitation from a diode pumped solid state laser (RL532C50, Renishaw, Inc.). Samples were held in a nitrogen-purged temperature-controlled stage (THMS600/TMS94/LNP94, Linkam Scientific Instruments Ltd). Excitation and collection of scattered light occurred through a 50× objective (Leica, NA=0.50). The laser power was set to 0.64 mW to exclude local heating effect. Collected spectra are typically consisted of the average of 20 integrations, where each integration was collected for 1 min.

IV. RESULTS AND DISCUSSIONS

We begin our discussions by investigating the structural properties of VO_2. The well-known experimental crystal structure of VO_2 [48] as described in Fig. 1. The unit cell contains 6 atoms for the R phase and 12 atoms for the M_1 phase in our considered experimental structure. As shown in Fig. 1(a), the V-V atoms form a periodic V chain with fixed V-V bond distance as 2.86 Å in the rutile structure, whereas there are significance differences in the arrangement of the V atoms along the rutile C_R axis in the M_1 phase, as demonstrated in Fig. 1(b). In this M_1 phase, the V atoms are arranged such a way that they form dimmer alternatively and tilt along the C_R axis, which leads to doubling of the unit cell volume of that for the R phase with V-V distance as 2.62 Å (bonding) and 3.16 Å (antibonding). With this understanding of available experimental crystal structure, we perform structure optimization of both the R and M1 phases of VO_2.

For structure optimization, we consider the optimization process, in which both the lattice parameters and atoms are allowed to move for searching the minimum energy configurations. First, we optimize the crystal structure of the R phase using different functionals without considering any spin

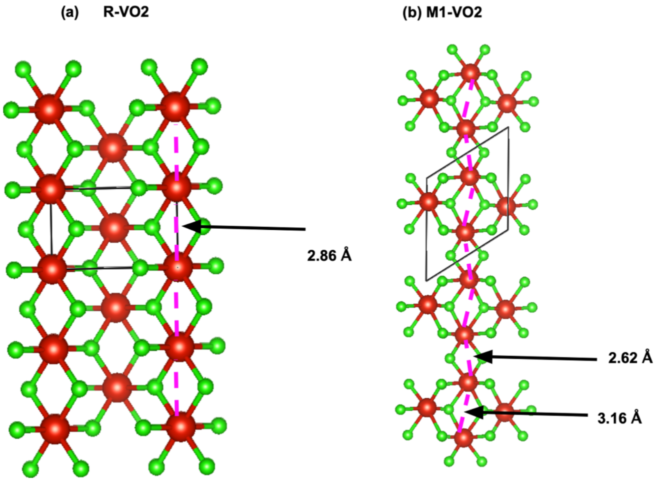

FIG. 1. The schematic of the experimental structures [48] for (a) rutile (R) and (b) monoclinic M1 phases of VO_2. Red and green spheres denote vanadium and oxygen atoms, respectively.

TABLE I. Optimized V-V distance for the rutile phase of VO_2 obtained from our calculations using different functional and spin ordering.

Functional	V-V distance
Exp. [48]	2.86
GGA (NM)	2.76
Ref. [34] (NM)	2.80
SCAN (NM)	2.77
SCAN (FM)	2.83
SCAN (AFM)	2.82

ordering (see Fig. 2) and compare it with experimental data [48] (see Fig. 1) and previously reported values [34] presented in Table I. For SCAN meta-GGA functional, the V-V pair distance changes from the experimental value 2.86 Å to 2.76 Å, whereas it is 2.77 Å for the GGA functional. We note that there is no significant changes in the results obtained from the SCAN meta-GGA and GGA functional. However, this is certainly not true for the case of M_1 phase excluding any spin ordering. Our calculations suggest that the optimization process is extremely sensitive to the functional used in the calculations as summarized in Table II. We find that the LDA functional completely fails to optimize the M_1 structure. We observe that the long V-V dimer and short V-V dimer distance becomes almost equal as 2.72 Å which imply that the M_1 structure reduces to the rutile like structure through the LDA optimization process. Hence, like electronic properties, our calculations reveal that the LDA is not applicable to determine the structural properties of the M_1 phase. The convergence of our LDA calculations have been carefully tested as discussed in Appendix A. However, the situation becomes better when the GGA is applied in our calculations. In the optimized M_1 structure based on the GGA functional, the long V-V dimer distance decreases to 3.0 Å from the experimental value 3.16 Å and short V-V dimer separation decreases to 2.59 Å from the experimental value 2.62 Å. Such drastic change in the dimmer distance clearly indicates that the M_1 structure again tends to go to the rutile phase through the optimization process. As has been already found [34], this failure of the LDA and GGA can be cured by the hybrid functional. To overcome this barrier, we have utilized SCAN meta-GGA functional for optimizing the M_1 structure. As summarized in Table II, in the SCAN optimized M_1 structure, the long V-V dimer nature survive as 3.16 Å which is very close to the value 3.14 Å as found in hybrid calculations [34] and exact as 3.16 Å as found in experiment [48]. The short V-V dimer using SCAN functional is found to be 2.47 Å which is also to 2.44 Å as found from the hybrid functional calculations. Thus, like hybrid functional, the optimized crystal structure using SCAN has all the expected features of the experimentally derived structure: All V-V chains of M_1 are found to be dimerized and canted along the rutile axis, whereas all V-V chains form straight undimerized one in the rutile phase. In addition, we have also performed structure optimization of both the rutile and M_1 phases of VO_2 including ferromagnetic (FM) and antiferromagnetic (AFM) spin ordering. The optimized FM-R and FM-M_1 are presented in Fig. 3. In the FM-M_1 optimized structure, the long V-V dimer distance deviates from the experimental value 3.16 Å to 2.93 Å, whereas the short V-V

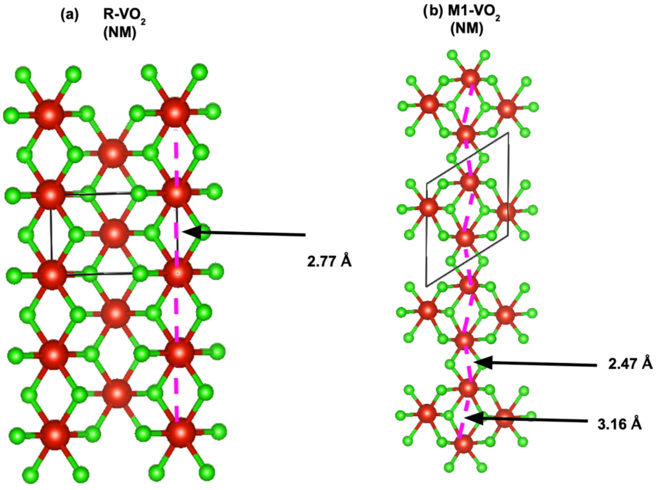

FIG. 2. The schematic of the optimized structures obtained from the non-spin-polarized calculations for (a) rutile (R) and (b) monoclinic M1 phases of VO_2. Red and green spheres denote vanadium and oxygen atoms, respectively.

TABLE II. Optimized long and short V-V dimer distances for the M_1 phase of VO_2 obtained from our calculations using different functional and spin ordering.

Functional	V-V dimer (long)	V-V dimer (short)
Exp. [48]	3.16	2.62
LDA (NM)	2.72	2.72
GGA (NM)	3.0	2.59
Ref. [34] (NM)	3.14	2.44
SCAN (NM)	3.16	2.47
SCAN (FM)	2.93	2.73
Hybrid (FM) [34]	2.94	2.69
SCAN (AFM)	3.07	2.80

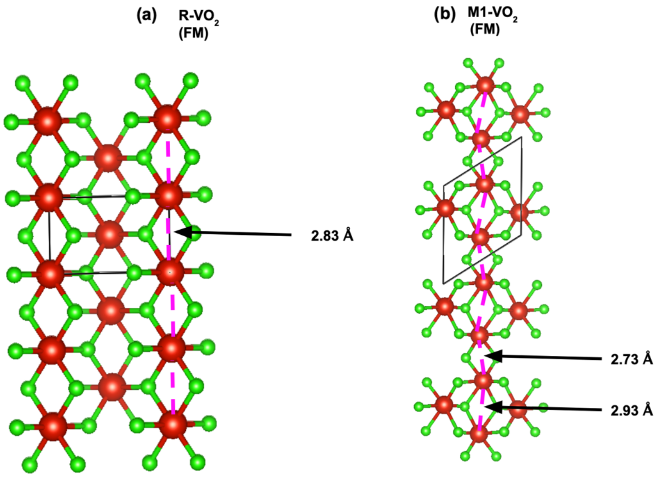

FIG. 3. The schematic of the optimized structures including ferromagnetic (FM) spin ordering for (a) rutile (R) and (b) monoclinic M1 phases of VO_2. Red and green spheres denote vanadium and oxygen atoms, respectively.

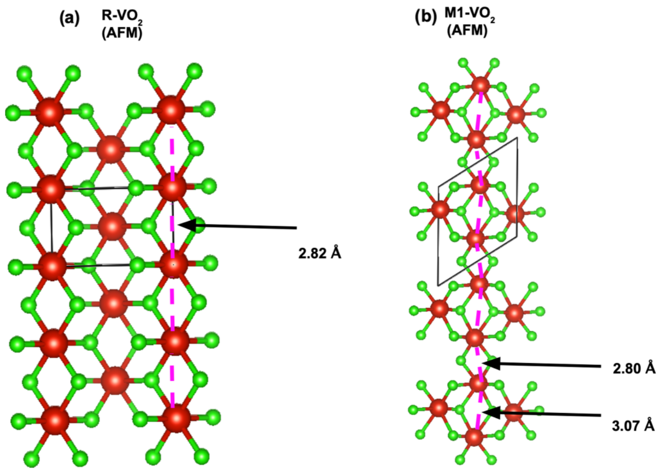

FIG. 4. The schematic of the optimized structures including antiferromagnetic (AFM) spin ordering for (a) rutile (R) and (b) monoclinic M1 phases of VO_2. Red and green spheres denote vanadium and oxygen atoms, respectively.

dimer distance becomes 2.73 Å from the experimental value 2.62 Å. As a result, the differences between the long and short V-V dimer distances deviates significantly in compare to the experimental value 0.69 Å to 0.2 Å. Therefore, in the optimized FM-M_1 VO_2, the corresponding structure tends to lose its dimer character. The obtained optimized structure of M_1 phase using the SCAN functional is in agreement with the previous Hybrid-functional calculations [34]. As we discussed in the SCAN predicted optimized structure, the long dimer value is found to be 2.93 Å which is very close to a value of 2.94 Å obtained from the Hybrid functional calculations. The predicted short dimer distance value is found to be 2.73 Å which is also close to the Hybrid functional predicted value as 2.69 Å. Thus, as discussed in the previous hybrid functional calculations, we also observe that the optimized FM-M_1 tends to reduce to the FM-R phase and survive in a new monoclinic phase with crystal structure in between M_1 and R which is named as M0 state. This M0 state is believed to be ferromagnetic in nature. Existing experimental data [56,57] at liquid-helium temperature also suggest possibility of such a phase. In the R-FM VO_2 the distance between V-V atoms becomes 2.83 Å from the experimental value 2.86 Å. However, in the AFM-M_1 optimized structures (see Fig. 4), the difference between the long V-V dimer and short V-V dimers remain more close to the experimental value compared to the FM-M_1 structure. In the AFM-M_1, the long V-V dimer value reduces to 3.07 Å from the experimental value 3.16 Å, whereas the short V-V dimer value becomes 2.82 Å from the experimental value 2.62 Å. So, the difference between long and short V-V dimer becomes 0.27 Å from the experimental value 0.69 Å. The V-V atom distance is found to be 2.82 Å in the optimized structure of AFM-R phase.

Structure optimizations of both the rutile and M_1 phases lead us to search for the energetically favorable phase of VO_2. Our non-spin-polarized calculations show that the low-temperature M_1 phase is energetically lowered than the high-temperature rutile phase by 22.18 meV per atom. In our antiferromagnetic (AFM) calculations, energy of the M_1 phase is found to be lower from the energy of the rutile phase by 27.92 meV per atom. The energy of the FM-R is found to be almost the same as the FM-M_1. In particular, the energy of the FM-M_1 is found to be higher compared to the FM-R phase by very small value as 1 meV per atom which is not sufficient to conclude that the FM-M_1 is not energetically favorable compared to the FM-R phase due to the numerical precision of DFT.

Next, we study the electronic properties of the M_1 phase focusing on the effect of the structural optimization on the electronic structure, to draw an accurate band theory picture of the M_1 phase. Fig. 5 presents the electronic density of states (DOS) based on our optimized structures. To treat the comparison on equal footing, we use SCAN functional in the calculation of electronic DOS from the structures that are obtained from different functional. As shown in the top panel of Fig. 5, there is no gap in the DOS corresponding to the LDA optimized structure. However, a pseudogap feature tends to emerge in the DOS of the GGA optimized structure as shown in the middle panel of the Fig. 5. Such small gap in the DOS with the GGA optimized structure was also previously reported and our calculations are consistent with these previous calculations [39,41]. Interestingly, we find a fully gapped spectrum with the SCAN optimized structure as displayed in the bottom panel of Fig. 5.

Figure 6 displays the variation of the density of states as a function of various values of short V-V dimer separation. As it is clearly seen from the top to bottom of this figure, there is no gap in the density of states for the V-V dimer distance as 2.59 Å. Interestingly, a finite gap emerges as the V-V dimer separation is varied from 2.59 Å to 2.48 Å. Thus, our calculations suggest that a gap can be opened up for the M_1 phase depending only on the structure property without considering any Hubbard onsite coulomb interactions. From our calculations, it is certainly clear that the role of Peierl's distortion cannot be neglected in determining the insulating nature of the M_1 phase. Such observations

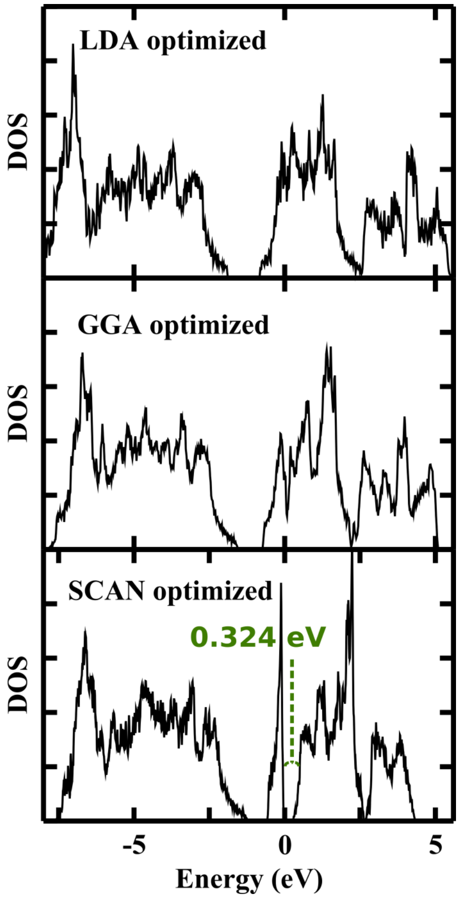

FIG. 5. Comparison of the electronic density of states (DOS) from the LDA, GGA, and SCAN optimized structures (from top to bottom of the figure) for the M_1-VO_2. Considering optimized structures with different functionals as input, all DOS calculations are performed by using SCAN. The gapped DOS with finite band gap value is only obtained from the SCAN optimized structure.

strongly suggest that the M_1 phase is not a conventional Mott insulator.

The next question we address here concerns the validity of the SCAN functional in describing the electronic properties of both the rutile and M_1 phases of VO_2, based on the obtained optimized structure. The calculated density of states considering various spin orderings are presented in Fig. 7. From the optimized structure considering nonmagnetic (NM) state, SCAN-based non-spin-polarized calculations predict the high temperature rutile phase as a metal and the low-temperature M_1 phase as an insulator [see Figs. 7(a) and 7(b)]. These findings are consistent with experiments. We note that previous calculations based on different functional fail to correctly describe both the phases of VO_2 simultaneously. For example, the LDA + U method find insulating nature of the rutile phase of VO_2 [38,58]. However, mBJ and hybrid functional as we discussed before can successfully describe both VO_2 phases. As we have already mentioned, mBJ cannot be utilized for calculating the forces and hybrid functional is computationally very expensive. Hence, they are not highly suitable particularly for phonon calculations of VO_2. In addition to nonmagnetic calculations, we have also performed spin-polarized calculations for computing the electronic properties of both the rutile and M_1 phases of VO_2. As shown in Fig. 7(f), we still find the insulating nature of the M_1 phase even if including antiferromagnetic spin ordering. Here, we note that previous LDA + U calculations [39] overestimate the band gap by finding the energygap value as 1.33 eV compared to the experimental value 0.6 eV, whereas our spin-polarized SCAN calculations yield bandgap value as 0.45 eV. At the same time, we also find the gapless metallic behavior of the rutile phase including the same AFM ordering [Fig. 7(e)]. However, our calculations using SCAN functional find both the rutile and M_1 phase as a half-metal for ferromagnetic spin ordering [Figs. 7(c) and 7(d)]. The obtained half-metallic nature instead of insulating of the FM-M_1 phase can be understood from the large variations of the V-V dimer in the optimized structure.

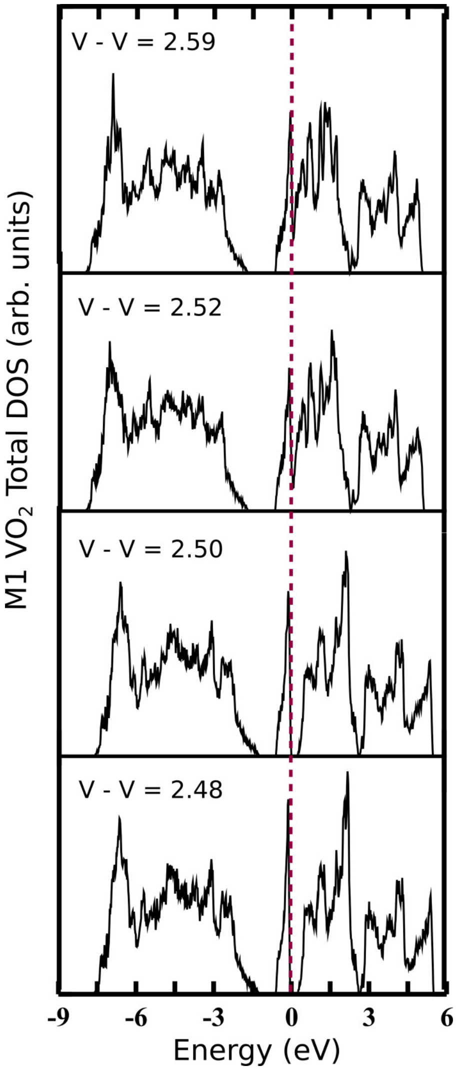

FIG. 6. The evolution of electronic density of states (DOS) with variation of short V-V dimer distance. In all four calculations of DOS, SCAN meta-GGA functional has been used. A gap opens at a critical value of the short V-V dimer distance suggesting that structure property of the M_1 phase play a significant role in controlling its insulating nature.

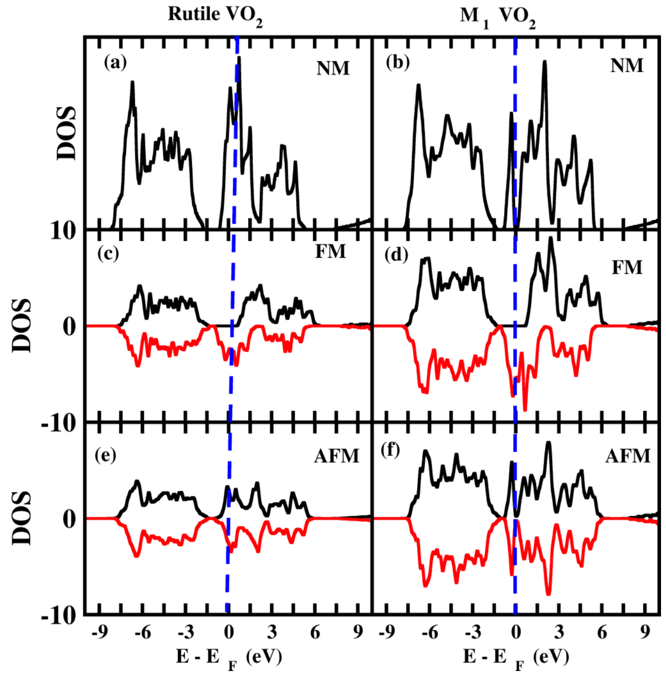

FIG. 7. Electronic density of states (DOS) for high-temperature rutile (R) and low-temperature monoclinic (M1) phases of VO$_2$ obtained using SCAN meta-GGA functional considering both the non-spin-polarized and spin-polarized calculations. In spin-polarized calculations, ferromagnetic (FM) and antiferromagnetic spin orderings are included.

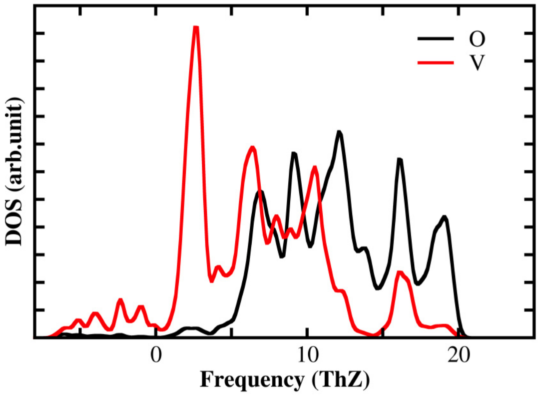

FIG. 9. Partial phonon density of states of the R-VO$_2$ calculated using the SCAN meta-GGA functional within the zero temperature and harmonic approximation. The low-frequency soft modes are mainly contributed by the V atoms.

Finally, we discuss the vibrational properties of both the rutile and M$_1$ phases of VO$_2$. Figure 8 shows the phonon dispersion curves of R-VO$_2$ using SCAN meta-GGA functional without including spin ordering. We have also performed same calculations using GGA functional. We find that the phonon dispersion for the rutile phase using the SCAN does not deviate significantly from the results using the GGA functional and observe the phonon softening instabilities in both the SCAN and GGA calculations. We consider the soft phonon modes are the unstable phonons whose frequencies are imaginary or negative. To identify which phonon modes are softening, we look into the partial phonon density density of states of the rutile phase. As shown in Fig. 9, the soft phonon modes are mainly originated from the V atoms. Such phonon softening of the rutile phase has already been reported before [39]. We note that zero temperature DFT calculations within harmonic approximations fail to predict stable rutile phase which is also expected since the rutile phase is stable only at high temperature. We obtain phonon softening at $\mathbf{q} = \mathbf{\Gamma}$, **M** and **X** which are in good agreement with previous GGA-based calculations [39]. Existing studies [59–64] suggest that the phonon softening at $\mathbf{q} = \mathbf{R}$ leads structural transition from the high temperature R structure to low-temperature M_1 structure. However, we have not found such well-known phonon softening at $\mathbf{q} = \mathbf{R}$ in our calculations using the SCAN. Moreover, phonon dispersion at the **R** point is found to be flat. Therefore, our analysis exclude the possibility of soft-mode transition at the $\mathbf{q} = \mathbf{R}$ wave vector based on symmetry argument and we believe that the lattice stability of the Rutile phase can be obtained if the effects of anharmonicity and temperature are included in the calculations which is also consistent as observed in experiment [41].

Besides partial phonon density of states, we also calculate total phonon density of states of rutile phase without considering any spin ordering as shown in Fig. 10. Followed by the dispersion, there are negative frequencies in the low energy region of the spectrum which is not shown here. Interestingly, we obtain a good agreement with the experimental phonon density of states. We note that the experimental phonon spectrum has been collected at temperature $T = 381$ K, whereas our calculations are limited to T = 0 K within harmonic approximations. Despite these limitations, we are able to capture qualitatively peak features of the experimental spectrum around 18, 33, 45, and 72 meV. We also observe that the height of the peak around 18 and 33 meV is more compared to the experimental one. This could be consequence of temperature effect. In addition, we also compare our results against previous calculations [41]. As we expected, we notice that the height of the peak decreases significantly particularly around 18 and 33 meV as

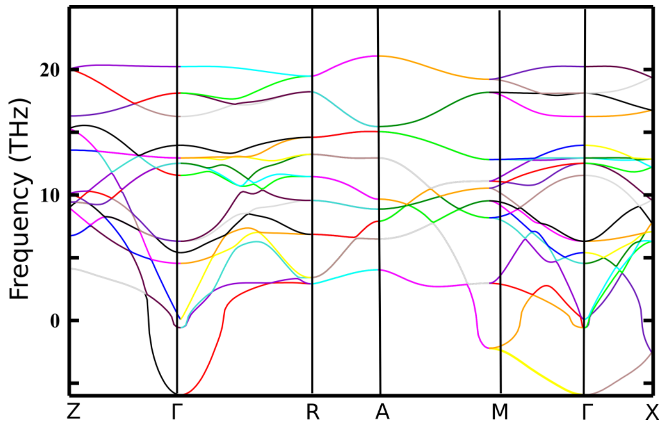

FIG. 8. Phonon dispersions of the R-VO$_2$ calculated using the SCAN meta-GGA functional within the zero temperature and harmonic approximation. Observe the phonon softening instability of the R phase at $q = \Gamma$, M, X.

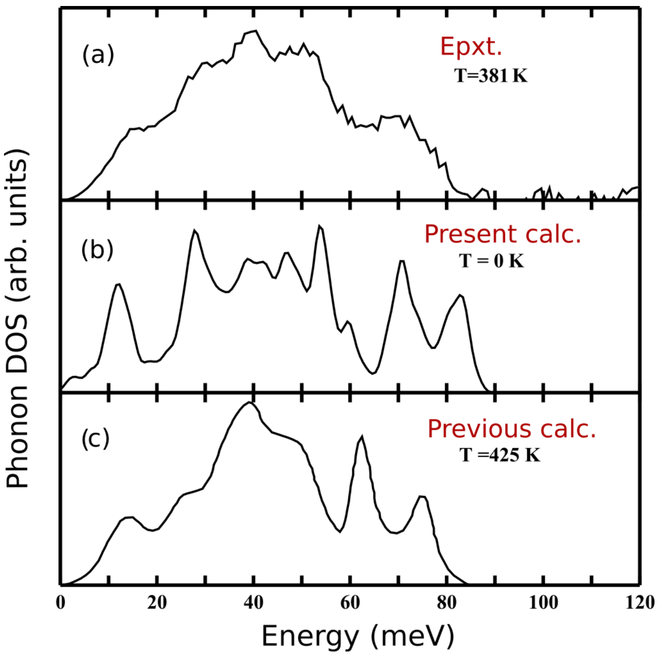

FIG. 10. The phonon density of states (PDOS) of the R-VO_2 obtained from zero temperature harmonic approximation-based calculations. Our computed PDOS for the R-VO_2 is in agreement with neutron scattering data [41].

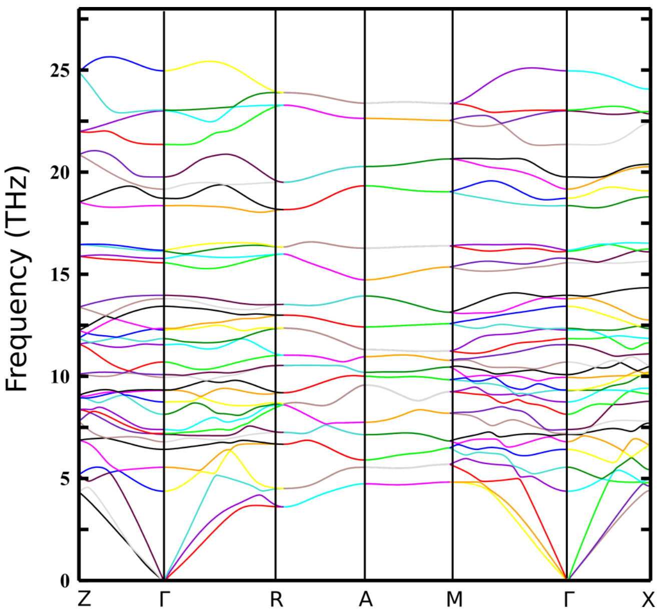

FIG. 11. Phonon dispersions of the M_1-VO_2 calculated using the SCAN meta-GGA functional within the zero temperature and harmonic approximation. The absence of any negative phonon frequencies (imaginary frequencies) suggesting the stability of the M_1 structure at low temperature.

temperature increases from 0 to 425 K. We also observe that our calculations are able to capture some features of the spectra that agree better with the experimental spectrum compared to previous theoretical calculations [41]. For example, the peak around 55 meV corresponding to the experimental DOS is shifted to around 65 meV in the DOS obtained from the previous calculations [41]. Also, previous calculations find DOS at the high-energy region remain around 83 meV, whereas the bandwidth of the experimental spectrum is larger. We note that the bandwidth of our calculated spectrum is much closer to the band width of the experimental DOS compared to previous finite temperature calculations. Although the high temperature rutile phase is believed to be anharmonic, the low-temperature M_1 phase is found to be highly harmonic. So, we expect our theoretical framework is more suitable for the M_1 phase, which is our next topic of discussion.

We have computed phonon dispersion of the M_1 phase based on the non-spin-polarized calculations as displayed in Fig. 11. The calculated dispersion curve for the M_1 phase is in good agreement with previous calculations [66]. As shown in Fig. 10, unlike rutile phase, there is no phonon softening which is consistent with experimental observations [41]. It confirms that this M1 phase is the stable structure of VO_2 at low temperature. Such structural information can be directly probed in Raman spectra. To understand that, a careful analysis of the phonon density of states can be good a starting point.

The phonon density of states of the M_1 phase is presented in Fig. 12. Followed by dispersion, there are no negative frequencies in the low-frequency region of our calculated phonon density of states which confirm the stability of the M_1 phase. Such dynamical stability for the AFM-M_1 phase is also predicted (see Appendix B). We compare our calculated phonon density of states at T =0 K with the phonon density states corresponding to $T = 298$ K obtained from experiment using neutron spectrometer as reported in Ref. [41]. We find our zero temperature calculations using SCAN functional successfully capture the experimentally observed phonon density of states at room temperature. To check the performance of SCAN against other functional, we also compare our results with

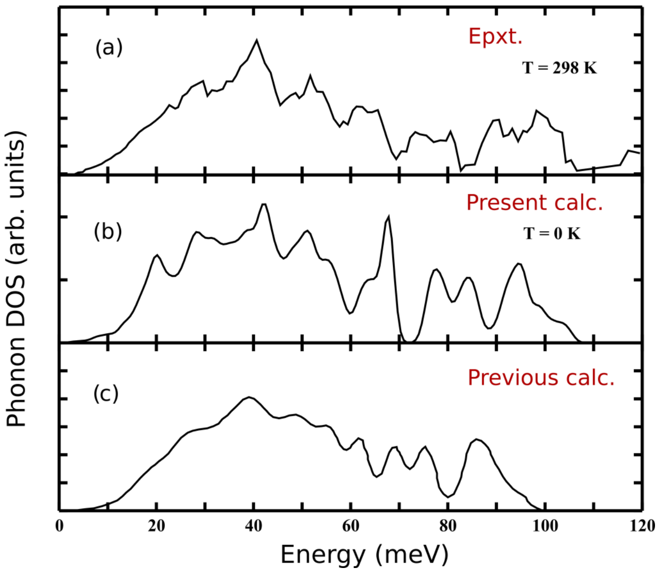

FIG. 12. The phonon density of states of the M_1-VO_2 obtained from zero temperature harmonic approximation-based calculations. Our computed PDOS of the M_1-VO_2 is in excellent agreement with the neutron scattering data [41].

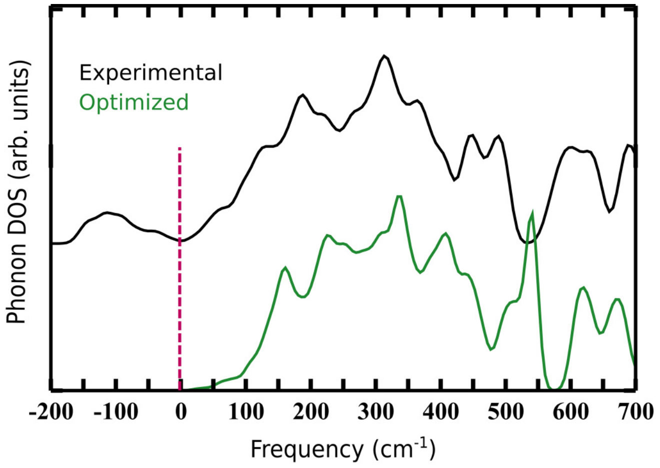

FIG. 13. Comparison of the phonon density of states of the M_1 phase of VO_2 obtained from the experimental structure (top) and the optimized structure (bottom). In both calculations, SCAN meta-GGA functional has been used. In the optimized structure, there is no negative frequency showing stability of the structure, however, the peak position deviates from the positions as found in Raman spectra. However, this agreement can be improved by considering experimental structure. But, there will be negative frequency associated with the phonon density of states if phonon calculations are done with out optimizing the experimental structure as expected.

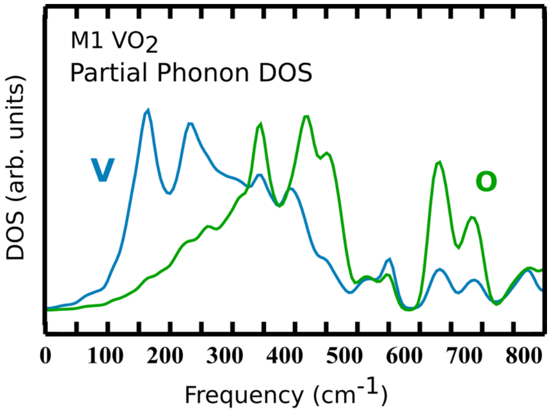

FIG. 14. Partial phonon density of states for V and O atoms of the M1 phase. The vibrational density of states at the low-frequency region around 190 cm^{-1} is mainly dominated by V atoms. However, at the high frequency region around 609 cm^{-1}, there is significant contribution from both the V and O atoms.

previous LDA + U calculations [41] as shown in the lower panel of Fig. 12. Comparison between the results obtained from SCAN and LDA + U clearly shows that the results obtained from SCAN serves better than the LDA + U. In particular, the peak features in the low-frequency region around 20 meV is more intense compared to the LDA + U results as observed in experiments.

We take a more closer look on the phonon density of states and study the effect of the V-V dimer on it. The role of V-V dimerization on the insulating behavior of the M1 phase is well understood now, whereas its effect on the lattice vibrations is still not extensively studied. Here, we aim to explore such physics. As we have already discussed that the V-V dimer distance deviates significantly from the experimental one, we compare phonon density of states of M_1 phase using both optimized and experimental structure as shown in Fig. 13. We observe that there are large number of negative frequencies in the low-frequency region of the phonon density of states derived from experimental structure as displayed in upper panel of Fig. 13, whereas there are no such negative frequencies in the low-frequency region of the phonon density of states considering optimized structure as shown in the lower panel of Fig. 13. The absence of such negative frequencies in the low-frequency region of the phonon density of states corresponding to optimized structure is well expected. Moreover, there are also other noticeable differences. There is a peak in the low-frequency region around 190 cm^{-1} and a peak in the high frequency region around 609 cm $^{-1}$ in the phonon density of states obtained from with out optimizing the structure. The low-frequency peak is mainly contributed from V-V pair and high frequency peak is originated from V-O pair which can be understood from Fig. 14. In addition, we investigate atomic displacement as presented in Fig. 15. To enable a proper comparison with Raman modes, these vibrational eigenvectors correspond to frequencies at the gamma point of two particular regions. Note that the low-frequency atomic displacement is governed by the vanadium dimer vibration while the high frequency eigenvector is a manifestation of oxygen atom displacements only. The positions of the peak and nature of the vibrations are in excellent agreement with the observed Raman spectra. However, the position of the peaks are shifted in the phonon density of states corresponding to optimized structure compared to without optimization one. We attribute this to the drastic change in the short V-V dimer distance that occurred in the optimization process Table II. We also note that peaks in the phonon DOS and Raman spectrum are not directly comparable. The Raman spectrum is only sensitive to zone-center Raman active modes, but the phonon DOS

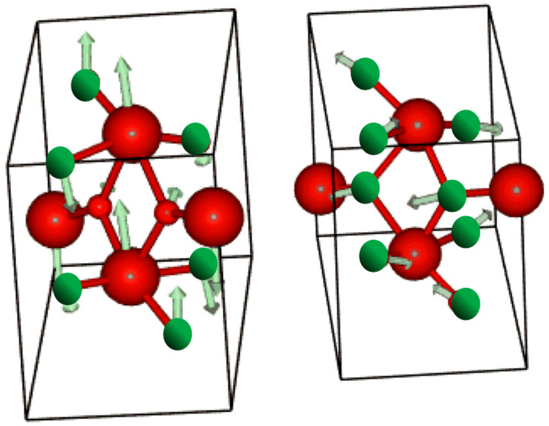

FIG. 15. Vibrational eigenvectors (phonon modes) with their corresponding frequency modes at 185.13 cm^{-1} for the left and 612.44 cm^{-1} for the right panel, respectively. The red spheres represent vanadium atoms and green spheres are oxygen. The vectors indicate the atomic displacements for each individual species corresponding to a snapshot of the vibrational movement. Images were generated using Ref. [65].

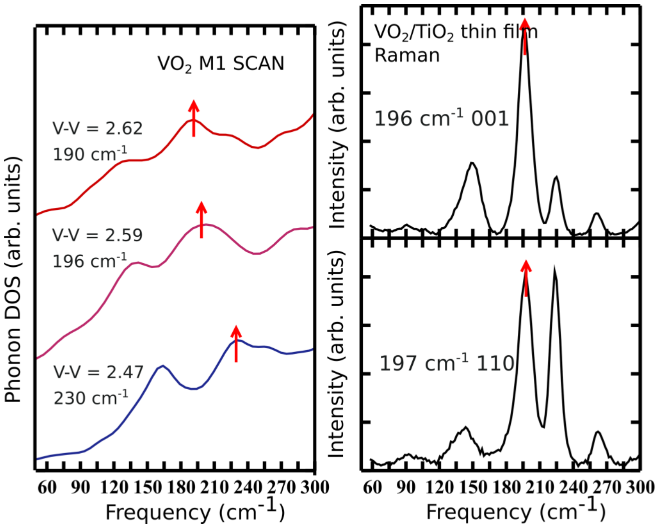

FIG. 16. Left panel: Evolution of the low-frequency peak around 190 cm^{-1} in the phonon density of states at different values of the V-V dimer distance of the M_1 bulk structure. Right panel: Evolution of the low-frequency peak around 196 cm^{-1} in the Raman spectrum at different values of strain on the 001 and 110 surface of M_1 structure. Our calculated value of the peak-position around 190 cm^{-1} is also in strong agreement with previous theoretical and experimental estimated value. First-principles-based simulations qualitatively capture the experimental observation of the Raman spectra at the low-frequency region with strain engineering.

integrates all phonon modes across the Brillouin zone, with peaks resulting from flat branches or van Hove singularities. Therefore, the meaning of peaks in the Raman spectrum and phonon DOS is different.

Modulation of the V-V dimer length can be accomplished with strain engineering. It has previously been shown in VO_2/TiO_2 epitaxial thin films that tensile strain on the c_R axis shifts the MIT mechanism toward bulklike characteristics largely driven by the Peierls physics while elongation of the c_R axis induces a larger influence from electron correlation or Mott physics [20–22]. However, due to the strong signal from the TiO_2 in Raman spectroscopy, the strain effect on the phonon modes has been misinterpreted [27]. Moreover, although strain has been accomplished on numerous substrates such as ZnO [67], Al_2O_3 [68], LSAT [69], and RuO_2 [70], the formation of rotational domains may complicate fundamental structural analysis in the investigation of the MIT. Like TiO_2, MgF_2 is isostructural to VO_2 in its high temperature phase, and exhibits weaker Raman response than TiO_2 substrate [71] and thus we selected it as the substrate for the epitaxial growth of VO_2 thin films. Fabrication of VO_2 on MgF_2 (001) induces the tensile strain of the c_R axis, while MgF_2 (110) films elongate the c_R axis [20,23]. Indeed, using Raman spectroscopy we observed spectral shift of the characteristic Raman peaks which represent V-V and V-O phonon modes. As shown in the right panels of Figs. 16 and 17, low-frequency peak is shifted from 196 cm $^{-1}$ to 197 cm $^{-1}$, whereas high frequency peak is shifted from 609 to 618 cm^{-1} with the application of strain. Such spectral displacement is shown in our calculated phonon density of states by manipulating V-V dimer. As presented in

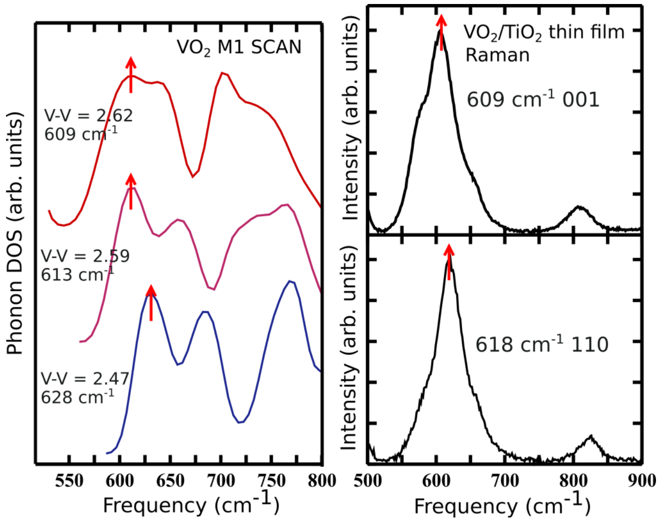

FIG. 17. Left panel: Evolution of the high-frequency peak around 609 cm^{-1} in the phonon density of states at different values of the V-V dimer distance of the M_1 bulk structure. Right panel: Evolution of the low-frequency peak around 609 cm^{-1} in the Raman spectrum at different values of strain on the 001 and 110 surface of M_1 structure. Our computed value of the peak position around 609 cm^{-1} is in strong agreement with previous theory and experimental calculated value. First-principles-based simulations qualitatively capture the experimental observation of the Raman spectra at the high frequency region with strain engineering.

the left panels of Figs. 16 and 17, the low-frequency peak has been shifted from 190 to 230 cm^{-1} as short dimer V-V distance is varied from 2.62 Å to 2.47 Å. Similarly, the high frequency peak is deviated from 609 to 628 cm $^{-1}$. Thus, our calculations qualitatively explain the effect of strain on the lattice vibrations as observed in our Raman experiments.

V. CONCLUSIONS

In this paper, we have computed structural, electronic and vibrational properties of the R and M_1 phases of VO_2 using first-principles calculations. We have employed the SCAN meta-GGA functional and successfully optimized the M_1 structure. The performance of the SCAN has been compared with various other functional in optimizing the M_1 structure. The SCAN optimized structure has been shown to produce consistent electronic properties including both the R and M_1 phases of VO_2. The low-temperature M_1 phase is found to be energetically favorable compared to the high temperature R phase. We have shown that the R phase is a metal, whereas the M_1 phase is found to be an insulator with finite band gap value. Moreover, we numerically demonstrate that a gap can be opened up as the V-V dimer length is varied without incorporating electronic correlations. Hence, our results strongly suggest that the M_1 phase is not a conventional Mott insulator given the sensitivity to the dimer distance to its electronic phase. The phonon softening related to the R phase and the phonon stiffening of the M_1 phase explain the structural phase transition from the R phase to M_1 as temperature is lowered. The V-V dimer has significant impact on both the electronic and vibrational properties of the M_1 phase. We show that the vibrational density of states significantly changes with the variation of the V-V dimer distance. Our calculated vibrational spectra are corroborated by previous neutron scattering experiment as well as our Raman experiment. In particular, our non-spin-polarized calculations of bulk VO_2 enable us to gain insight into the structural properties of strained VO_2 as found in our Raman experiment.

In addition, we have also performed spin-polarized calculations of both the Rutile and M_1 phases of VO_2. Our calculations reveal that the AFM-M_1 is energetically stable over the AFM-R phase. Both the FM-M_1 and FM-R phases of VO_2 are found to be almost the same in energy and predicted to be half-metals. The AFM-M_1 is found to be insulating, whereas the AFM-R phase is predicted to be appropriate metal. Again, such AFM-M_1 phase is also demonstrated to be dynamically stable. On the contrary, the FM-M_1 phase is shown to be dynamically unstable. Overall, our work suggests that the SCAN can be utilized for investigating phonon properties of related materials and such work is in progress.

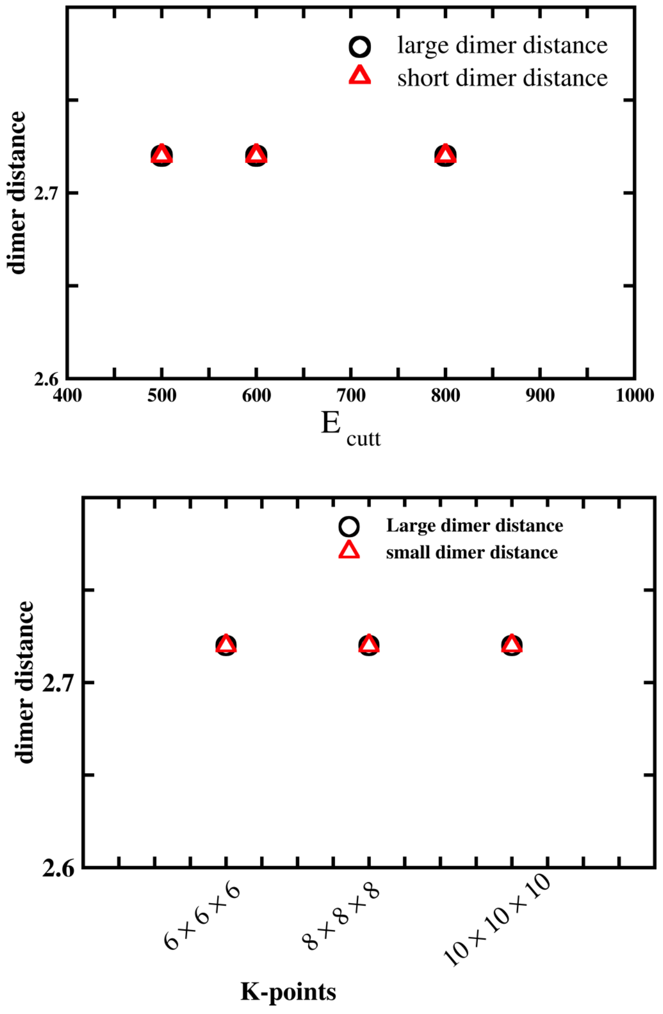

FIG. 18. Convergence of our LDA results against K-mess and energy cutoff (E_{cut}).

ACKNOWLEDGMENTS

We thank Dr. Christopher N. Singh for helpful discussions in our theoretical calculations, Dr. David J. Gosztola and Dr. Benjamin T. Diroll for assistance with Raman microscopy measurements. This paper is based on the work supported by the Air Force Office of Scientific Research under Award No. FA9550-18-1-0024 administered by Dr. Ali Sayir. For the film synthesis we acknowledge the National Science Foundation [Platform for the Accelerated Realization, Analysis, and Discovery of Interface Materials (PARADIM)] under Cooperative Agreement No. DMR-1539918. This research used resources of the Center for Nanoscale Materials, an Office of Science user facility, was supported by the U.S. Department of Energy, Office of Science, Office of Basic Energy Sciences, under Contract No. DE-AC02-06CH11357. Moreover, this work made use of the Cornell Center for Materials Research Shared Facilities which are supported through the NSF MRSEC program (Grant No. DMR-1719875). G.J.P.F. acknowledges doctoral degree grant support (Grant No. E0565514) from the Comisión Fulbright Ecuador in conjunction with the Ecuadorian national science department Secretaría de Educación Superior, Ciencia, Tecnología e Innovación (Senescyt).

APPENDIX A: CONVERGENCE TEST OF OUR LDA RESULTS

We have checked convergence of our results obtained from the LDA against increasing K mesh as well as energy cut off. As shown in Fig. 18 (top), we have performed calculations for various values of energy cutoff (E_{cut}) ranging from 400 to

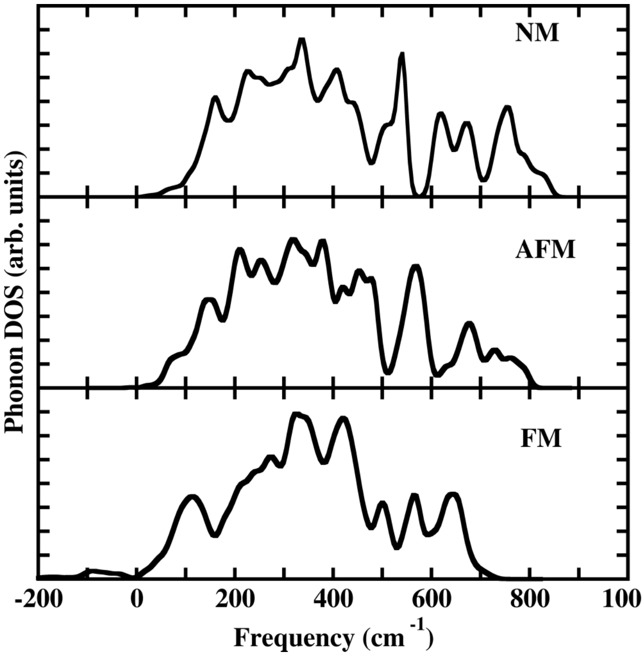

FIG. 19. Calculated phonon density of states for the M_1 phase of VO_2 using the SCAN meta-GGA functional considering ferromagnetic (FM) and antiferromagnetic (AFM) spin ordering.

800 eV, but we have not observed any change in our results. In addition, we have tested our calculations for increasing K-mesh values from $6 \times 6 \times 6$ to $10 \times 10 \times 10$. Again, we have not found any change in our results as shown at the bottom of Fig. 18. Thus, convergence of our LDA results have been confirmed and overall we find the LDA fails to describe the correct physics of the M_1 phase which is not surprising because it has been already confirmed in a number of previous studies [15,28].

APPENDIX B: SPIN-POLARIZED PHONON CALCULATIONS FOR THE M_1 PHASE

We have computed the phonon density of states of both the AFM-M_1 and FM-M_1 phases of VO_2 (see Fig. 19). We do not observe negative frequencies in our calculated phonon density of states for the AFM-M_1. The absence of any negative frequencies indicates the dynamical stability of the AFM-M_1 phase. Moreover, our calculations also suggest that FM-M_1 is not dynamical stable.

[1] F. J. Morin, Phys. Rev. Lett. **3**, 34 (1959).
[2] E. Strelcov, Y. Lilach, and A. Kolmakov, Nano Lett. **9**, 2322 (2009).
[3] T. D. Manning, I. P. Parkin, M. E. Pemble, D. Sheel, and D. Vernardou, Chem. Mater. **16**, 744 (2004).
[4] S. Kim, J. Park, J. Woo, C. Cho, W. Lee, J. Shin, G. Choi, S. Park, D. Lee, B. H. Lee, and H. Hwang, Microelectron. Eng. **107**, 33 (2013).
[5] S. H. Shin, T. Halpern, and P. M. Raccah, J. Appl. Phys. **48**, 3150 (1977).
[6] W. L. Lim, E. J. Moon, J. W. Freeland, D. J. Meyers, M. Kareev, J. Chakhalian, and S. Urazhdin, Appl. Phys. Lett. **101**, 143111 (2012).
[7] Z. Yang, C. Ko, and S. Ramanathan, Annu. Rev. Mater. Res. **41**, 337 (2011).
[8] A. Zylbersztejn and N. F. Mott, Phys. Rev. B **11**, 4383 (1975).
[9] T. M. Rice, H. Launois, and J. P. Pouget, Phys. Rev. Lett. **73**, 3042 (1994).
[10] T. J. Huffman, C. Hendriks, E. J. Walter, J. Yoon, H. Ju, R. Smith, G. L. Carr, H. Krakauer, and M. M. Qazilbash, Phys. Rev. B **95**, 075125 (2017).
[11] S. Biermann, A. Poteryaev, A. I. Lichtenstein, and A. Georges, Phys. Rev. Lett. **94**, 026404 (2005).
[12] M. W. Haverkort, Z. Hu, A. Tanaka, W. Reichelt, S. V. Streltsov, M. A. Korotin, V. I. Anisimov, H. H. Hsieh, H.-J. Lin, C. T. Chen, D. I. Khomskii, and L. H. Tjeng, Phys. Rev. Lett. **95**, 196404 (2005).
[13] C. Weber, D. D. O’Regan, N. D. M. Hine, M. C. Payne, G. Kotliar, and P. B. Littlewood, Phys. Rev. Lett. **108**, 256402 (2012).
[14] A. Cavalleri, T. Dekorsy, H. H. W. Chong, J. C. Kieffer, and R. W. Schoenlein, Phys. Rev. B **70**, 161102(R) (2004).
[15] R. M. Wentzcovitch, W. W. Schulz, and P. B. Allen, Phys. Rev. Lett. **72**, 3389 (1994).
[16] J. B. Goodenough, J. Solid State Chem. **3**, 490 (1971).
[17] K. Liu, S. Lee, S. Yang, O. Delaire, and J. Wu, Materials Today **21**, 875 (2018).
[18] D. Wickramaratne, N. Bernstein, and I. I. Mazin, Phys. Rev. B **99**, 214103 (2019).
[19] P. Ganesh, F. Lechermann, I. Kylänpää, J. T. Krogel, P. R. C. Kent, and O. Heinonen, Phys. Rev. B **101**, 155129 (2020).
[20] N. F. Quackenbush, H. Paik, M. J. Wahila, S. Sallis, M. E. Holtz, X. Huang, A. Ganose, B. J. Morgan, D. O. Scanlon, Y. Gu, F. Xue, L.-Q. Chen, G. E. Sterbinsky, C. Schlueter, T.-L. Lee, J. C. Woicik, J.-H. Guo, J. D. Brock, D. A. Muller, D. A. Arena, D. G. Schlom, and L. F. J. Piper, Phys. Rev. B **94**, 085105 (2016).
[21] G. J. Paez, C. N. Singh, M. J. Wahila, K. E. Tirpak, N. F. Quackenbush, S. Sallis, H. Paik, Y. Liang, D. G. Schlom, T.-L. Lee, C. Schlueter, W.-C. Lee, and L. F. J. Piper, Phys. Rev. Lett. **124**, 196402 (2020).
[22] W. C. Lee, M. J. Wahila, S. Mukherjee, C. N. Singh, T. Eustance, A. Regoutz, H. Paik, J. E. Boschker, F. Rodolakis, T. L. Lee, D. G. Schlom, and L. F. Piper, J. Appl. Phys. **125**, 082539 (2019).
[23] E. Evlyukhin, S. A. Howard, H. Paik, G. J. Paez, D. J. Gosztola, C. N. Singh, D. G. Schlom, W.-C. Lee, and L. F. J. Piper, Nanoscale **12**, 18857 (2020).
[24] G. I. Petrov, V. V. Yakovlev, and J. Squier, Appl. Phys. Lett. **81**, 1023 (2002).
[25] K. Shibuya and A. Sawa, Jpn. J. Appl. Phys. **53**, 3 (2014).
[26] K. Okimura, N. Hanis Azhan, T. Hajiri, S. I. Kimura, M. Zaghrioui, and J. Sakai, J. Appl. Phys. **115**, 153501 (2014).
[27] M. Yang, Y. Yang, Bin Hong, L. Wang, K. Hu, Y. Dong, H. Xu, H. Huang, J. Zhao, H. Chen, L. Song, H. Ju, J. Zhu, J. Bao, X. Li, Y. Gu, T. Yang, X. Gao, Z. Luo, and C. Gao, Sci. Rep. **6**, 23119 (2016).
[28] Z. Zhu and U. Schwingenschlögl, Phys. Rev. B **86**, 075149 (2012).
[29] A. Continenza, S. Massidda, and M. Posternak, Phys. Rev. B **60**, 15699 (1999).
[30] M. Gatti, F. Bruneval, V. Olevano, and L. Reining, Phys. Rev. Lett. **99**, 266402 (2007).
[31] R. Sakuma, T. Miyake, and F. Aryasetiawan, Phys. Rev. B **78**, 075106 (2008).
[32] M. S. Laad, L. Craco, and E. Müller-Hartmann, Phys. Rev. B **73**, 195120 (2006).
[33] V. Eyert, Phys. Rev. Lett. **107**, 016401 (2011).
[34] S. Xu, X. Shen, K. A. Hallman, R. F. Haglund, and S. T. Pantelides, Phys. Rev. B **95**, 125105 (2017).
[35] H. Zheng and L. K. Wagner, Phys. Rev. Lett. **114**, 176401 (2015).
[36] W. R. Mondal, N. S. Vidhyadhiraja, T. Berlijn, J. Moreno, and M. Jarrell, Phys. Rev. B **96**, 014203 (2017).
[37] W. R. Mondal, T. Berlijn, M. Jarrell, and N. S. Vidhyadhiraja, Phys. Rev. B **99**, 134203 (2019).
[38] M. A. Korotin, N. A. Shorikov, and V. I. Anisimov, Phys. Metals Metallograph (USSR) **94**, 17 (2002).
[39] S. Kim, K. Kim, C.-J. Kang, and B. I. Min, Phys. Rev. B **87**, 195106 (2013).

[40] T. A. Mellan, H. Wang, U. Schwingenschlögl, and R. Grau-Crespo, Phys. Rev. B **99**, 064113 (2019).

[41] J. D. Budai, J. Hong, M. E. Manley, E. D. Specht, C. W. Li, J. Z. Tischler, D. L. Abernathy, A. H. Said, B. M. Leu, L. A. Boatner, R. J. McQueeney, and O. Delaire, Nature **515**, 535 (2014).

[42] C. N. Berglund and H. J. Guggenheim, Phys. Rev. **185**, 1022 (1969).

[43] K. Kosuge, J. Phys. Soc. Jpn. **22**, 551 (1967).

[44] T. Kong, M. W. Masters, S. L. Bud'ko, and P. C. Canfield, APL Mater. **3**, 041502 (2015).

[45] J. P. Pouget, H. Launois, T. M. Rice, P. Dernier, A. Gossard, G. Villeneuve, and P. Hagenmuller, Phys. Rev. B **10**, 1801 (1974).

[46] R. Grau-Crespo, H. Wang, and U. Schwingenschlögl, Phys. Rev. B **86**, 081101(R) (2012).

[47] I. Kylänpää, J. Balachandran, P. Ganesh, O. Heinonen, P. R. C. Kent, and J. T. Krogel, Phys. Rev. Materials **1**, 065408 (2017).

[48] V. Eyert, Ann. der Phys. **11**, 650 (2002).

[49] G. Kresse and J. Furthmüller, Phys. Rev. B **54**, 11169 (1996).

[50] G. Kresse and J. Furthmüller, Comput. Mater. Sci. **6**, 15 (1996).

[51] J. P. Perdew, K. Burke, and M. Ernzerhof, Phys. Rev. Lett. **77**, 3865 (1996).

[52] J. Sun, A. Ruzsinszky, and J. P. Perdew, Phys. Rev. Lett. **115**, 036402 (2015).

[53] A. Togo and I. Tanaka, Scr. Mater. **108**, 1 (2015).

[54] K. Parlinski, Z. Q. Li, and Y. Kawazoe, Phys. Rev. Lett. **78**, 4063 (1997).

[55] H. Paik, J. A. Moyer, T. Spila, J. W. Tashman, J. A. Mundy, E. Freeman, N. Shukla, J. M. Lapano, R. Engel-Herbert, W. Zander, J. Schubert, D. A. Muller, S. Datta, P. Schiffer, and D. G. Schlom, Appl. Phys. Lett. **107**, 163101 (2015).

[56] K. Kosuge, Y. Ueda, S. Kachi, T. Shinjo, T. Takada, and M. Takano, J. Solid State Chem. **23**, 105 (1978).

[57] J. Pouget, P. Lederer, D. Schreiber, H. Launois, D. Wohlleben, A. Casalot, and G. Villeneuve, J. Phys. Chem. Solids **33**, 1961 (1972).

[58] G.-H. Liu, X.-Y. Deng, and R. Wen, J. Mater. Sci. **45**, 3270 (2010).

[59] J. R. Brews, Phys. Rev. B **1**, 2557 (1970).

[60] C. J. Hearn, J. Phys. C **5**, 1317 (1972).

[61] D. B. McWhan, M. Marezio, J. P. Remeika, and P. D. Dernier, Phys. Rev. B **10**, 490 (1974).

[62] H. Terauchi and J. B. Cohen, Phys. Rev. B **17**, 2494 (1978).

[63] F. Gervais and W. Kress, Phys. Rev. B **31**, 4809 (1985).

[64] S. M. Woodley, Chem. Phys. Lett. **453**, 167 (2008).

[65] Visualize phonon vibrational modes, https://henriquemiranda.github.io/phononwebsite/.

[66] S. Lee, K. Hippalgaonkar, F. Yang, J. Hong, C. Ko, J. Suh, K. Liu, K. Wang, J. J. Urban, X. Zhang, C. Dames, S. A. Hartnoll, O. Delaire, and J. Wu, Science **355**, 371 (2017).

[67] F. J. Wong, Y. Zhou, and S. Ramanathan, J. Cryst. Growth **364**, 74 (2013).

[68] L. L. Fan, S. Chen, Y. F. Wu, F. H. Chen, W. S. Chu, X. Chen, C. W. Zou, and Z. Y. Wu, Appl. Phys. Lett. **103**, 131914 (2013).

[69] Y. Liu, S. Niu, T. Orvis, H. Zhang, H. Zhao, H. Wang, and J. Ravichandran, J. Vacuum Sci. & Tech. A **36**, 061506 (2018).

[70] S. Fischer, J.-O. Krisponeit, M. Foerster, L. Aballe, J. Falta, and J. I. Flege, Cryst. Growth Des. **20**, 2734 (2020).

[71] K. Shibuya, J. Tsutsumi, T. Hasegawa, and A. Sawa, Appl. Phys. Lett. **103**, 021604 (2013).